chemosensors

MDPI

Article

Efficient Cataluminescence Sensor for Detecting Methanol Based on $NiCo_2O_4$//MIL-Ti_{125} Polyhedral Composite Nano-Materials

Hongyan Wang [1,*], Ziyu Shao [1], Mao Cai [2], Guoji Shi [2] and Bai Sun [2,3,*]

[1] Department of Radiation Oncology, The First Affiliated Hospital of Anhui Medical University, Hefei 230022, China
[2] Anhui Institute of Urban and Rural Green Development and Urban Renewal, College of Environment and Energy Engineering, Anhui Jianzhu University, Hefei 230601, China
[3] Environmental Materials and Pollution Control Laboratory, Hefei Institute of Physical Science, Chinese Academy of Sciences, Hefei 230031, China
* Correspondence: whhy5000@163.com (H.W.); bsun@iim.ac.cn (B.S.)

Abstract

Since methanol has a significant health hazard due to its inherent toxicity, it is urgent to develop a method capable of rapid, sensitive, and continuous monitoring of methanol. The present study successfully synthesized a $NiCo_2O_4$/MIL-Ti_{125} composite material and conducted a comprehensive analysis of its effectiveness for the detection of methanol employing cataluminescence (CTL) technology. The findings demonstrated that the composite material displays marked CTL in response to methanol, showcasing notable sensitivity, selectivity, and stability. The composite's heterogeneous structure significantly improves the adsorption and reaction efficiency of methanol and further reduces the sensor's working temperature. Under the optimal conditions of 215 °C and a flow rate of 300 mL/min, the CTL signal intensity is governed by the equation $Y = 10.388X - 4.473$ ($R^2 = 0.982$), with a detection limit as low as 0.431 ppm. The $NiCo_2O_4$/MIL-Ti_{125} sensor exhibits high selectivity towards methanol. In addition, a relative standard deviation (RSD) of 4.95% demonstrates its excellent stability. Utilizing X-ray photoelectron spectroscopy (XPS), the study investigated the impact of elemental valence changes on the CTL process. We believe that the $NiCo_2O_4$/MIL-Ti_{125} composite material, as a high-performance low-temperature CTL methanol sensor, is promising for applications.

Keywords: $NiCo_2O_4$/MIL-Ti_{125} composite; CTL; methanol detection; sensitivity; selectivity; stability

check for updates

Received: 13 January 2025
Revised: 27 March 2025
Accepted: 1 September 2025
Published: 5 September 2025

Citation: Wang, H.; Shao, Z.; Cai, M.; Shi, G.; Sun, B. Efficient Cataluminescence Sensor for Detecting Methanol Based on $NiCo_2O_4$//MIL-Ti_{125} Polyhedral Composite Nano-Materials. *Chemosensors* **2025**, *13*, 339. https://doi.org/10.3390/chemosensors13090339

Copyright: © 2025 by the authors. Licensee MDPI, Basel, Switzerland. This article is an open access article distributed under the terms and conditions of the Creative Commons Attribution (CC BY) license (https://creativecommons.org/licenses/by/4.0/).

1. Introduction

Methanol, as a pivotal organic chemical raw material [1], plays a significant role across various sectors, including chemical engineering, energy, and textiles. Its broad applications encompass the production of chemicals such as formaldehyde, acetic acid, and methyl tert-butyl ether [2]. Methanol is attracting interest not only as an alternative to energy and automotive fuels but also for its high combustion efficiency and relatively clean emission profile. Moreover, its significance in C1 chemistry is escalating, with increasing interest in processes that synthesize ethylene glycol, acetaldehyde, and ethanol from methanol [3]. Despite these beneficial applications, the toxicity of methanol cannot be overlooked. The toxicity of methanol primarily stems from its metabolites, formaldehyde and formic acid, which are 20 and 6 times more toxic than methanol [4], respectively. In the human body, methanol is initially converted to formaldehyde by alcohol dehydrogenase and then rapidly

transformed into formic acid by aldehyde dehydrogenase [5]. The slower metabolism of formic acid makes it the principal toxicant in methanol poisoning, which can lead to severe health issues, including blurred vision, potential blindness, and damage to the central nervous system [6]. Prolonged exposure to high concentrations of methanol may also be carcinogenic. Currently, maximum permissible concentration of methanol in shop air is 35 ppm [7], so it is important to develop efficient methods for the detection of it.

The main methods in the field of methanol detection include gas chromatography (GC) [8], Ultraviolet–Visible Spectrophotometry (UV-Vis) [9] and chemical titration (e.g., redox titration) [10]. Although these methods have achieved some research results, they have some limitations. For example, GC relies on complex pre-treatment and expensive equipment [11]; UV-Vis is susceptible to interference from co-existing components [12]; and chemical methods are difficult to achieve real-time monitoring. CTL, as an emerging detection technology, has become a hot research topic for trace gas detection due to the characteristics of no external light source, high sensitivity and real-time monitoring [13]. However, the traditional CTL sensors need to be improved in terms of insufficient selectivity, poor long-term stability, and so on. By constructing heterogeneous composites of metal–organic frameworks (MOFs) and metal oxides, the molecular sieve effect of MOFs and the catalytic activity of metal oxides can be synergistically utilised to significantly enhance the sensor performance [14]. Therefore, the development of highly active sensitive materials is an effective way to solve this problem.

MOFs are key materials for CTL signal enhancement due to their tunable pore structure and surface chemistry. Taking the titanium-based MOF material MIL-Ti_{125} as an example, its high specific surface area, abundant active sites, and excellent carrier transport ability make it outstanding in the field of photocatalysis and sensing [15,16]. These properties not only enhance its utility in photocatalysis but also position it as a promising candidate for sensing applications, such as detecting volatile organic compounds (VOCs) in breath-based diagnostics and serving as a luminescent sensor for biomarkers [17,18]. Sheng et al. prepared a modified titanium dioxide photocatalyst, NH_2-MIL-125(Ti), using an in situ acid etching strategy, and an in-depth study of the properties of this material demonstrated that it possesses significant adsorption capacity and excellent light-absorption properties [19]. This approach aligns with the broader trend of MOF-based composites in addressing challenges such as selective VOC detection and low-concentration biomarker analysis. For instance, recent studies have leveraged MOFs for lung cancer screening by targeting breath VOCs and developed Ni(II)-MOF sensors with dual-function capabilities for detecting nitrotyrosine biomarkers, further underscoring the potential of MIL-Ti_{125} in advancing multifunctional sensing platforms [20]. $NiCo_2O_4$, a binary transition metal oxide with a spinel structure [21], has attracted considerable interest due to its superior theoretical capacity, low cost, ecological abundance, ease of synthesis, and excellent electrochemical activity. The material exhibits superior electrical conductivity compared to individual metal oxides, such as nickel oxide (NiO) and cobalt oxide (CoO). $NiCo_2O_4$ can be synthesized in various morphologies by adjusting hydrothermal reaction conditions, with nanosheet arrays showing highly ordered structures and good conductivity, providing abundant active sites and facile pathways for electron and electrolyte ion transfer [22].

The complexation of MIL-Ti_{125} with metal oxides and the construction of heterojunctions have been employed to enhance the catalytic efficiency of MIL-Ti_{125}-based composites. Within composite materials, heterojunctions facilitate efficient charge carrier separation, thereby enhancing the efficiency of catalytic luminescence. For instance, the formation of a heterojunction between Bi_2O_3 and TiO_2 through chemical bonding has been shown to improve the separation of electrons and holes, thereby enhancing CTL efficiency [23]. Liu et al. utilized a hydrothermal method to fabricate nano-array structured NiO/$NiCo_2O_4$ het-

erojunctions, which can facilitate interfacial charge transfer and enhance the electrochemical activity for oxygen evolution [24]. Xu et al. facilitated the growth of TiO_2 on NH_2-MIL-Ti_{125} (NM-$_{125}$), achieving a highly efficient interfacial effect, thereby demonstrating superior photocatalytic NO activity [25]. Huang et al. synthesized BiOBr/NH-MIL-Ti_{125} using an alkaline solution exfoliation method, featuring a layered Z-scheme heterojunction with a more intimate face-to-face interfacial contact that significantly enhances migration efficiency and separation capabilities [26].

In this study, composites consisting of $NiCo_2O_4$ and MIL-Ti_{125} metal–organic frameworks (MOFs) were prepared and investigated as sensing materials for the CTL method for the detection of methanol. The composite was designed to enhance oxygen adsorption and improve the conversion efficiency of reactants, thereby increasing sensing efficiency, through the construction of heterostructures. Material characterization techniques including scanning electron microscopy (SEM), X-ray diffraction (XRD), Fourier-transform infrared spectroscopy (FT-IR), X-ray photoelectron spectroscopy (XPS), and Brunauer–Emmett–Teller (BET) surface area and porosity analysis were utilized to analyze the material properties. Additionally, the study explored the impact of various factors on methanol CTL intensity, including sensor selectivity, working temperature, carrier gas flow rate, and analyte concentration. This research not only optimizes the performance of MIL-Ti_{125}-based CTL sensors but also provides a feasibility study on enhancing sensing efficiency by constructing heterojunctions between materials.

2. Experimental Materials and Methods

2.1. Fabrication of $NiCo_2O_4$/MIL-Ti_{125} Composite Material

The fabrication of the $NiCo_2O_4$/MIL-Ti_{125} composite material was executed in this study, with the following detailed procedure:

The synthesis of MIL-Ti_{125} commenced with 3 g of terephthalic acid (H_2BDC, 18 mmol) dissolved in a mixed solvent system comprising 1.56 mL of titanium butoxide (TBT, 4.5 mmol), 54 mL of N,N-dimethylformamide (DMF), and 6 mL of anhydrous methanol. The mixture was magnetically stirred for one hour, achieving a homogeneous solution, which was then transferred to a 100 mL Teflon-lined autoclave and reacted at 160 °C for 20 h. Post-reaction, the product underwent centrifugal filtration through DMF and methanol three times and was dried in an oven at 80 °C to yield a white powder of MIL-Ti_{125}.

Next, the production of $NiCo_2O_4$ involved dissolving 1.5 mmol of $CoCl_2{\cdot}6H_2O$, 0.75 mmol of $NiCl_2{\cdot}6H_2O$, and 45 mmol of urea in 20 mL of ultrapure water, followed by magnetic stirring at room temperature for 30 min. After stirring, the solution was transferred to a 50 mL Teflon-lined stainless-steel autoclave and maintained at 120 °C for 6 h. Upon completion of the reaction, the solution was allowed to cool naturally to room temperature, followed by centrifugal filtration through ultrapure water and ethanol three times, and dried at 60 °C for 12 h.

Finally, the $NiCo_2O_4$/MIL-Ti_{125} composite was fabricated by dispersing MIL-Ti_{125} and $NiCo_2O_4$ at a 3:1 mass ratio in 50 mL ethanol, followed by ultrasonication to achieve homogeneous dispersion. The mixture was magnetically stirred at 60 °C for 1 h to form a homogeneous mixture, cooled to room temperature, and washed with ethanol. The resulting purple suspension was dried in an oven at 60 °C for 2 h to obtain the $NiCo_2O_4$/MIL-Ti_{125} composite material. This methodical approach ensures the precise assembly of each component, culminating in a composite material that is well-suited for applications in catalytic luminescence sensing of methanol.

2.2. Main Analytical Instruments

The main analytical instruments employed in this study are listed below: The surface morphology of the synthesized nanomaterials was characterized using a scanning electron microscope (Zeiss, Jena, Germany). Chemical composition analysis of the prepared materials was conducted with an energy-dispersive spectrometer (AURIGA, Jena, Germany). Phase and crystal structure of the materials were examined by an X-ray diffractometer (Panalytical, Almelo, The Netherlands). Surface functional groups of the material samples were analyzed using a Fourier transform infrared spectrometer (NEXUS-870, Thermo Fisher Corporation, Waltham, MA, USA).

2.3. CTL Devices and Detection Methods

In this study, a weak luminescence detection apparatus (BPCL-1), Figure 1, was employed to investigate the CTL properties of the $NiCo_2O_4$/MIL-Ti_{125} composite material. This approach allowed for a thorough examination of the material's response to catalytic stimuli, providing valuable insights into its potential applications in sensing technologies. The system consists of three main components: a reaction chamber with a ceramic heating rod coated with the composite material and a quartz tube for gas flow, a temperature and flow rate control unit to maintain stable experimental conditions, and a photoelectric detection and data processing system with a high-sensitivity photomultiplier tube (PMT) capable of converting weak luminescence signals into electrical signals for amplification and detection. The BPCL-1 instrument, when connected to a computer, provides high sensitivity and stability for analyzing luminescence signals with long-term stability better than 1.5% RSD. To evaluate the sensor dynamics, response time and recovery time were defined and measured accordingly. The response time is defined as the time taken for the CTL signal to increase from the steady baseline level to maximum value upon analyte introduction. Conversely, the recovery time refers to the time required for the signal to decrease from the maximum value back to the steady baseline level after the analyte supply is terminated. These parameters reflect the efficiency of gas interaction with the sensing material. During the experimental procedure, the sensing material was initially dissolved in ultrapure water and subsequently applied evenly onto a cylindrical ceramic heating rod. This rod was then subjected to evaporation in a vacuum oven set at 60 °C to form a uniform coating. Once the ceramic heating rod was placed within a quartz tube, analyte vapor was introduced into the reaction chamber, with precise control over temperature and flow rate variables to mimic real-world working conditions. Ultimately, the CTL signal was detected by the BPCL apparatus and subsequently converted into analyzable data, facilitating further analysis and interpretation of the experimental results.

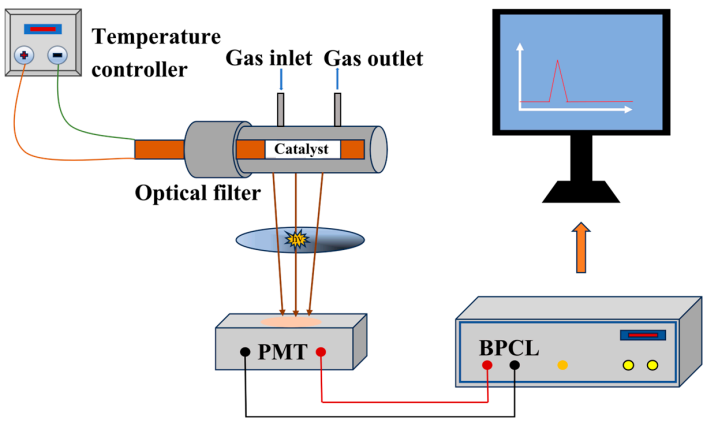


Figure 1. Schematic diagram of the BPCL-1 sensor unit.

The methanol concentration in this experiment was 156.16 ppm. The concentration of the target gas is calculated from the saturated vapor pressure equation [27]:

$$C = \frac{V_i \times P_0}{V_c \times P_a}$$

where C is the target concentration of VOC, V_i is the volume of VOC inhaled into the syringe, V_c is the volume of the laboratory, P_0 is the vapor pressure of the gas to be tested at room temperature, and P_a is the standard atmospheric pressure.

3. Results and Discussion

3.1. Material Characterization

3.1.1. SEM Analysis

The $NiCo_2O_4$/MIL-Ti_{125} composite material was synthesized via a hydrothermal method, with its SEM images presented in Figure 2a–d. The images reveal that $NiCo_2O_4$ consists of numerous nanorods assembled into microspheres, while MIL-Ti_{125} exhibits a tetradecahedral structure, which possesses a large specific surface area conducive to the adsorption of $NiCo_2O_4$ microspheres on its surface, thereby enhancing the adsorption of reactants. The presence of heterostructures around the $NiCo_2O_4$/MIL-Ti_{125} composite material, as observed in Figure 2a–d, the metal oxide $NiCo_2O_4$ is organically combined with the metal framework of MIL-Ti_{125}, potentially accelerating the migration of charge carriers during the reaction process and enhancing the sensitivity of the composite material.

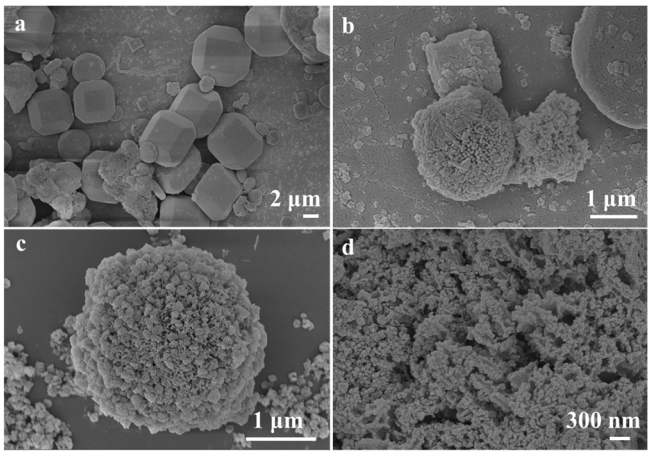


Figure 2. (**a**–**d**) SEM images of $NiCo_2O_4$//MIL-Ti_{125}.

To investigate the distribution and content relationship of elements within the material, energy-dispersive EDS mapping was conducted, as shown in Figure 3a depicts the selected area for testing, while Figure 3b–f illustrate the distribution and content of C, O, Ti, Ni, and Co elements, respectively. It is evident that the Ti element is the most abundant compared to Co and Ni. Analysis of the elemental distribution within the tested area confirms the presence of characteristic elements Ti, Co, and Ni in the $NiCo_2O_4$/MIL-Ti_{125} material, which are uniformly distributed. Combining this with the EDS spectrum (Figure 4) and the elemental content table, the relative atomic percentages of Ti, Co, and Ni in the $NiCo_2O_4$/MIL-Ti_{125} composite are determined to be 7.48%, 3.81%, and 1.77%, respectively. The Ti element is the most abundant, suggesting its significant role in the composite material, with Co and Ni elements present in lesser amounts.

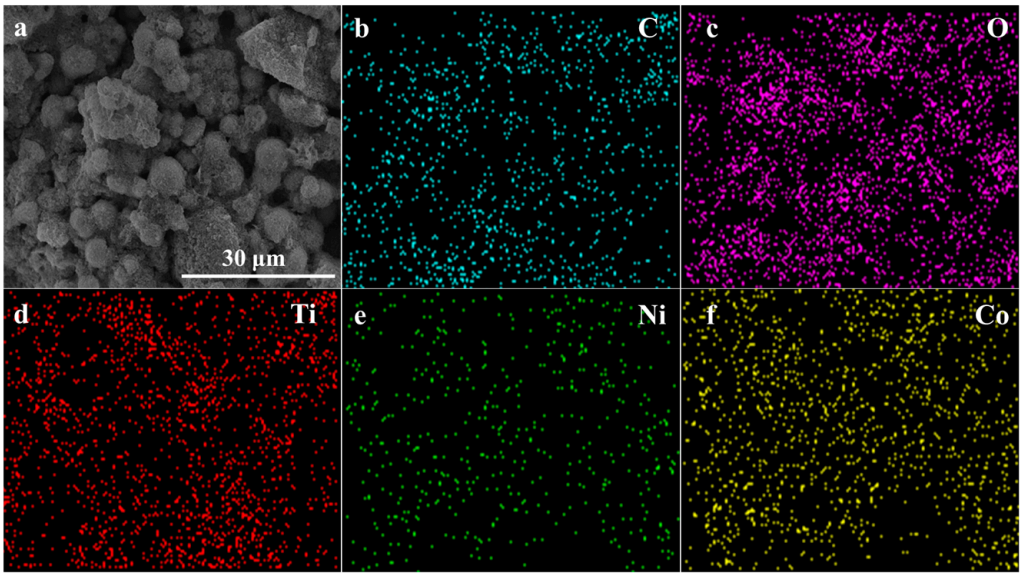


Figure 3. (**a**) SEM image; EDS mapping images of (**b**) C, (**c**) O, (**d**) Ti, (**e**) Ni and (**f**) Co.

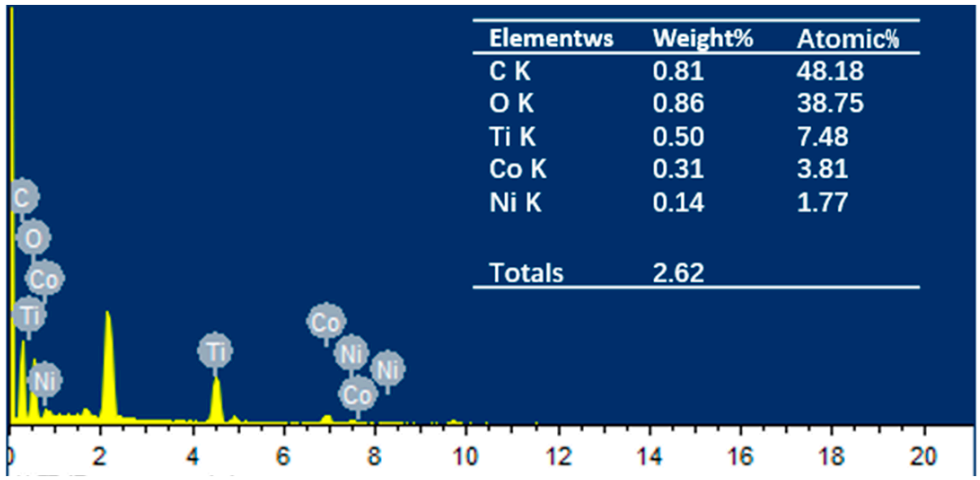


Figure 4. EDS energy spectra and corresponding elemental content percentages of $NiCo_2O_4$/MIL-Ti_{125}.

3.1.2. XRD Phase Analysis

In the investigation of the crystal structure of the $NiCo_2O_4$/MIL-Ti_{125} composite material, XRD analysis was conducted, with the results depicted in Figure 5. The diffraction peaks observed at specific 2θ angles are located at 2θ = 7.56°, 9.91°, 15.52°, 16.62°, 25.75°, 33.76°, and 39.82°. These peaks correspond to the (001), (002), (111), (220), and (222) planes of $NiCo_2O_4$, and the (100) and (110) planes of MIL-Ti_{125}, respectively. The XRD pattern matches the standard cards of JCPDS NO. 20-0781 for $NiCo_2O_4$ and JCPDS NO. 18-1586 for MIL-Ti_{125}, confirming the presence of both phases in the composite material synthesized via the hydrothermal method. Additionally, energy-dispersive EDS analysis revealed elemental compositions that are in good agreement with the expected values, further attesting to the successful synthesis and high purity of the $NiCo_2O_4$/MIL-Ti_{125} composite. The XRD pattern indicates that the peak intensities for MIL-Ti_{125} and $NiCo_2O_4$ are relatively low, with the peaks for $NiCo_2O_4$ being sharper than those for MIL-Ti_{125}, suggesting a more ordered stacking structure for $NiCo_2O_4$.

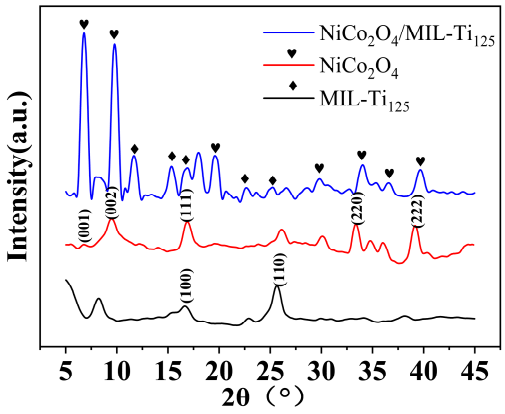


Figure 5. XRD pattern of $NiCo_2O_4$/MIL-Ti_{125} composites.

3.1.3. FT-IR Analysis

Figure 6 presents the FT-IR spectrum of the $NiCo_2O_4$/MIL-Ti_{125} composite material. The FT-IR analysis of the $NiCo_2O_4$/MIL-Ti_{125} composite reveals a series of characteristic absorption peaks that provide detailed information about the functional groups present in the material. Specifically, the absorption peak at 1700 cm^{-1} corresponds to the C=O stretching vibration of the H_2BDC ligand in MIL-Ti_{125} [28]. Additionally, the symmetric stretching vibration of the carboxylate group (OCO) at 1400 cm^{-1} and the stretching vibration of the ester C-O at 1050 cm^{-1} both originate from MIL-Ti_{125}. The vibrational absorption peaks in the range of 400–800 cm^{-1} are attributed to the Ti-OC stretching vibration [29], a signature functional group of MIL-Ti_{125}. Further analysis solidifies the presence of the Ti-OC functional group. These characteristic vibrational frequencies provide crucial spectroscopic evidence for the structural and performance analysis of the composite material.

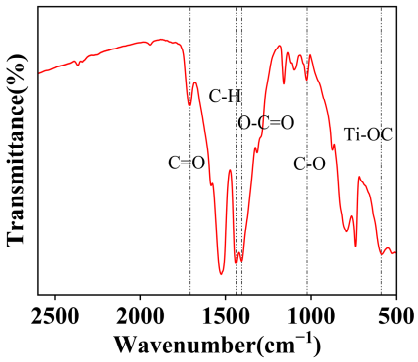


Figure 6. FT-IR patterns of $NiCo_2O_4$//MIL-Ti_{125}.

3.1.4. BET Analysis

Figure 7 presents the adsorption isotherms and pore size distribution analyses of $NiCo_2O_4$ and the $NiCo_2O_4$/MIL-Ti_{125} composite material. The analysis of the specific surface area and pore size of these two samples shows that the adsorption isotherms of these two materials belong to type-IV isotherms, with H3 hysteresis loops [30], indicating the presence of mesopores in the materials. The increase in specific surface area leads to a corresponding rise of the number of active sites [31]. This finding is consistent with previous results obtained through SEM analysis, which identified polyhedral structures in the composite material and hierarchical microspherical structures in $NiCo_2O_4$. The adsorption capacity had not reached saturation at a relative pressure of 1, suggesting the presence of pores within the adsorbent.

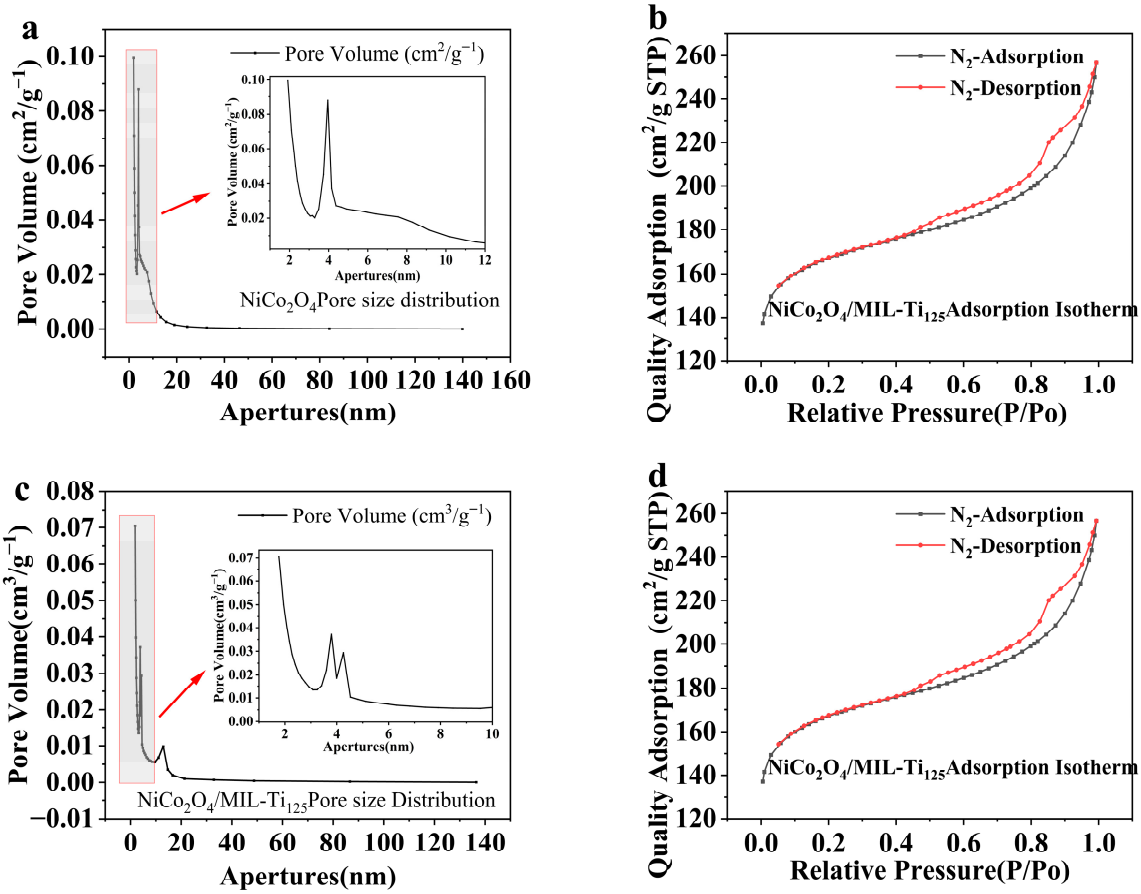


Figure 7. Adsorption isotherms and pore size analysis plots for (**a**,**b**) $NiCo_2O_4$ (The small figure is an enlarged view of the shaded area); (**c**,**d**) $NiCo_2O_4$/MIL-Ti_{125}.

Figure 7b,d indicate that the pore sizes of both materials are primarily distributed between 1 and 10 nm, suggesting that the materials are predominantly microporous and mesoporous with relatively large pore sizes. BET characterization data revealed that the BET specific surface areas of $NiCo_2O_4$ and $NiCo_2O_4$/MIL-Ti_{125} are 301.7857 m^2/g and 556.3482 m^2/g, respectively.

3.2. Effect of MIL-Ti_{125} Modification on $NiCo_2O_4$ CTL Performance

This study investigated the performance of $NiCo_2O_4$ and $NiCo_2O_4$/MIL-Ti_{125} composite materials as sensitive materials for CTL sensors (Figure 8). The experimental setup involved a flow rate of 350 mL/min, a temperature of 215 °C, and a reaction environment with a methanol concentration of 200 ppm. Data analysis showed that both sensors have a response time of 10 s and a recovery time of approximately 97 s, demonstrating comparable response and recovery rates. In contrast, the $NiCo_2O_4$ sensor requires additional time to begin recovery after the response ends, whereas the luminescence signal intensity of the $NiCo_2O_4$/MIL-Ti_{125} sensor is significantly higher, approximately double that of $NiCo_2O_4$, and exhibits more stable CTL. This can be attributed to the distinctive structural characteristics of MIL-Ti_{125}, whose titanium metal framework readily forms heterostructures with various semiconductor materials upon contact, thereby enhancing adsorption capabilities, improving charge carrier transport efficiency, and facilitating the CTL reaction [32]. Additionally, the composite's pore size distribution and specific surface area substantially affect the catalytic efficacy. The BET specific surface area of the $NiCo_2O_4$/MIL-Ti_{125} composite is 556.3482 m^2/g, surpassing that of the individual component, $NiCo_2O_4$, at 301.7857 m^2/g, likely contributing to its enhanced selectivity. The

increased specific surface area and optimal pore size distribution offer more active sites for methanol molecules, thereby augmenting selective adsorption and catalytic efficiency for methanol, endowing the $NiCo_2O_4$/MIL-Ti_{125} CTL sensor with superior selectivity in methanol detection. Consequently, the addition of MIL-Ti_{125} not only enhances the sensitivity of the sensor but also strengthens its stability, thereby improving the overall performance of the $NiCo_2O_4$/MIL-Ti_{125} composite material as a CTL sensor.

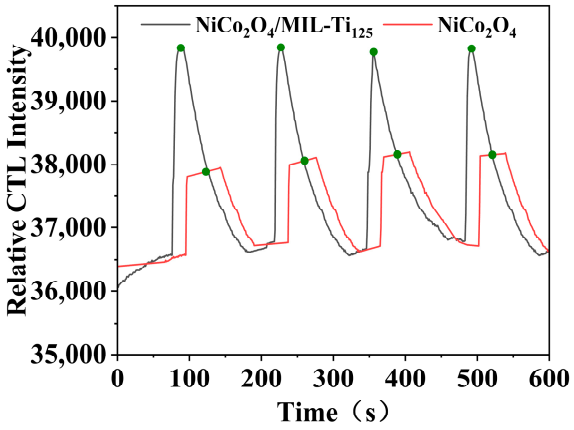


Figure 8. Comparison of CTL signal intensities of $NiCo_2O_4$, $NiCo_2O_4$/MIL-Ti_{125} (Working condition: concentration, 156.16 ppm; flow rate, 350 mL/min; temperature, 215 °C; The green dots in the figure indicate the turning point between sensor response time and recovery time).

3.3. Effect of Working Temperature on CTL

Temperature is a critical parameter in the study of CTL sensor performance [33], significantly affecting the catalytic activity of materials and the response characteristics of the sensor. The experiments conducted investigated the impact of temperature on the CTL sensor performance of $NiCo_2O_4$/MIL-Ti_{125} composite materials.

Under a flow rate of 350 mL/min and a methanol concentration of 156.16 ppm, the impact of temperature on sensor performance was analyzed by comparing the CTL signal strength and the signal-to-noise ratio (S/N). The S/N ratio is a critical parameter for assessing sensor performance, as the presence of background noise in sensors can attenuate the output signal, thereby affecting the CTL reaction's signal strength [34]. The experimental results (Figure 9) indicate that as temperature increases, the CTL signal strength continuously increases; however, due to the presence of sensor noise, the S/N ratio begins to decline after reaching its peak value. This noise is typically generated by dark current, which is the current observed under conditions devoid of light penetration and is an undesired factor in the imaging process of sensors. As temperature increases, the noise signal also intensifies. Considering the impact of the S/N ratio, continuously increasing the temperature does not yield the best performance for the sensor.

The $NiCo_2O_4$/MIL-Ti_{125} CTL sensor works at a lower experimental temperature compared to other material sensors, which not only reduces the impact of noise due to temperature in experiments but also extends the service life of the sensor (Table 1). Despite not having the quickest recovery time, considering all factors, the $NiCo_2O_4$/MIL-Ti_{125} CTL sensor performs the best in this experiment. Therefore, 215 °C was chosen as the experimental temperature. Reaction temperature is an important factor that limits the use conditions and stability of CTL and sensors [35]. Many sensing materials require a certain temperature to be activated, but an increase in temperature greatly affects the stability of the instrument itself. The development of composite materials has successfully addressed this issue by integrating and amplifying the advantages of different materials through

material combination, greatly expanding the application potential of composite materials in the field of sensors.

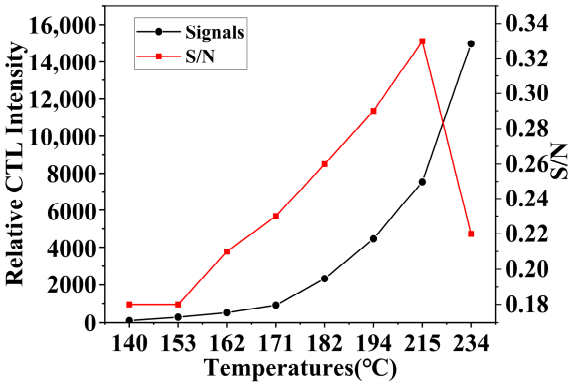


Figure 9. Effect of working temperature on CTL signal intensity and S/N (Working condition: concentration, 156.16 ppm; flow rate, 350 mL/min).

Table 1. Selected experimental temperatures and response and recovery times of methanol sensors based on different sensing materials.

Sensing Materials	Analyte	Working Temperature (°C)	Limit of Detection (ppm)	Flow Rate (mL/min)	Response Time (s)	Recovery Time (s)	Reference
Cobalt-doped SnO_2 thick films	Methanol Analyte	200	100	200	90	200	[36]
ZnO thin film		275	50	150	280	135	[37]
Flower-like In_2O_3 micro rods		300	5	100	15	20	[38]
ZnO nanorods		300	10	80	216	405	[39]
CuO thin film		350	20	120	235	225	[40]
Aluminium doped NiO nanotubes		325	2	180	199	15	[41]
$NiCo_2O_4$/MIL-Ti_{125}		215	0.4	50	10	97	this Study

3.4. Effect of Carrier Gas Flow Rate on CTL Intensity

In the realm of CTL sensor performance, the flow rate is a pivotal parameter [42], significantly influencing the response characteristics of the sensors. Within experimental contexts, the flow rate influences not merely the contact efficiency between the target analyte and the catalyst but also indirectly affects the CTL process. Optimizing the flow rate is essential for enhancing the sensitivity. In the study of the $NiCo_2O_4$/MIL-Ti_{125} CTL sensor, the impact of flow rate on the CTL performance of methanol vapor was meticulously analyzed (Figure 10). The experimental findings demonstrate that, under conditions of 215 °C temperature and a methanol concentration of 156.16 ppm, the CTL signal intensity and the signal-to-noise ratio (S/N) of the sensor vary with the increase in flow rate within the range of 100–500 mL/min. The $NiCo_2O_4$/MIL-Ti_{125} sensor achieved its peak S/N ratio at a flow rate of 300 mL/min, indicating an optimal balance between the flow rate and the sensor's sensitivity to methanol vapor. Conversely, excessively slow flow rates may diminish mass transfer efficiency, consequently attenuating the CTL signal. Conversely, an excessively rapid flow rate may lead to analyte molecules undergoing incomplete reactions, thereby also diminishing the CTL signal strength. Thus, identifying an optimal flow rate that harmonizes the contact duration and reaction efficiency between analyte molecules and the catalyst is essential for CTL sensor performance. The effect of flow rate on CTL sensor performance is multifaceted: it exerts an indirect influence on the CTL process through its impact on the contact efficiency and reaction duration between analyte molecules and the catalyst. Optimizing the flow rate can significantly augment the sensitivity of CTL sensors, thereby elevating their overall performance.

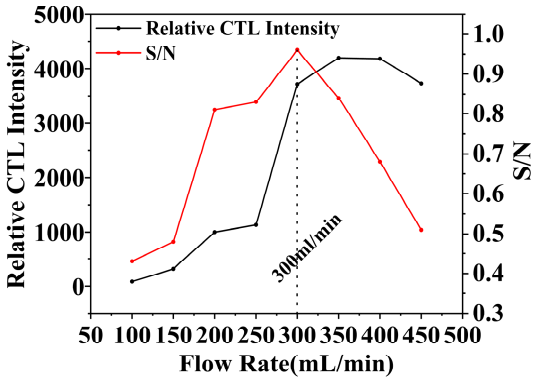
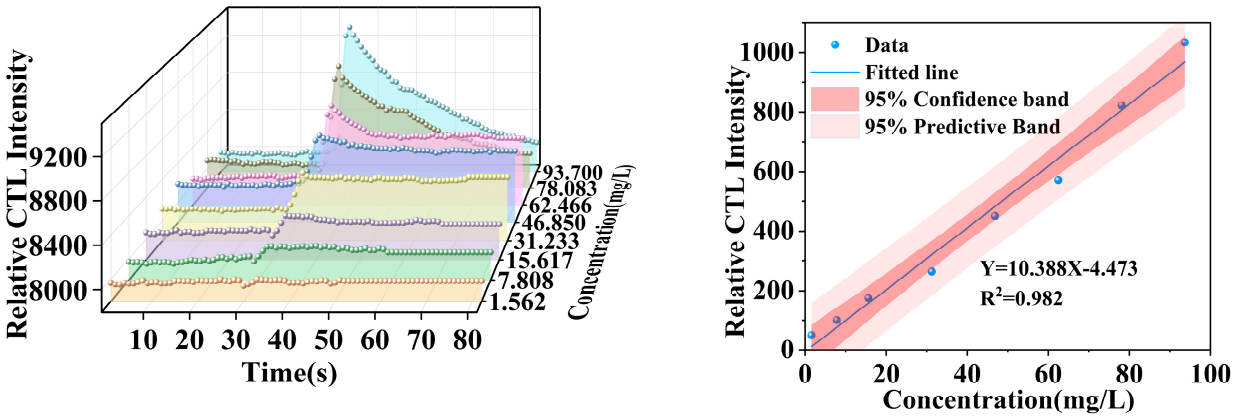


Figure 10. Effect of carrier gas flow rate on CTL signal intensity and S/N (Working condition: concentration, 156.16 ppm; temperature, 215 °C).

3.5. The Correspondence Between the CTL Intensity and the Concentration of the Analyte

Under optimized conditions, this investigation thoroughly examined the relationship between the signal strength of a CTL sensor based on the $NiCo_2O_4$/MIL-Ti_{125} composite material and methanol concentrations spanning 1 to 156.16 ppm. The experimental findings, as depicted in Figure 11a, reveal significant variations in the signal strength across varying methanol concentrations. The CTL signal intensity augments with increasing methanol concentrations, exhibiting the sensor's high sensitivity to methanol concentration fluctuations. At elevated concentrations, the CTL signal intensity is observed to augment, potentially due to enhanced interaction between methanol molecules and the catalyst, thereby escalating the CTL reaction rate.



(**a**) (**b**)

Figure 11. (**a**) CTL intensities corresponding to different concentrations of methanol; (**b**) methanol concentration versus signal intensity curves (Working condition: flow rate, 300 mL/min; temperature, 215 °C).

Furthermore, the data reveal that the $NiCo_2O_4$/MIL-Ti_{125} attains its peak signal-to-noise ratio (S/N) at a flow rate of 300 mL/min. The CTL sensor fabricated from the $NiCo_2O_4$/MIL-Ti_{125} composite material demonstrates exceptional performance in detecting methanol concentrations, with a strong correlation between signal strength and methanol concentration, and attains a high S/N ratio even at lower flow rates, showcasing its potential and advantages for practical applications [43]. Figure 11b displays the fitted curve of CTL signal strength as a function of methanol concentration, depicting a relationship, yet the signal strength is proportional to methanol concentration. The linear equation that models this relationship is $Y = 10.388\ X - 4.473$ ($R^2 = 0.982$), where Y represents the relative CTL intensity elicited by the composite material's surface in response to methanol across eight

gradient concentrations in parallel experiments, X denotes the methanol concentration, and R signifies the correlation coefficient. The detection limit was ascertained utilizing a prescribed formula.

$$D = 3N \times \frac{Q}{I} \quad (1)$$

where Q is the minimum inlet concentration within the concentration detection range; N is the noise of the reaction at the minimum inlet concentration; I is the response signal value corresponding to the minimum inlet concentration within the detection range. The detection limit is calculated to be 0.431 ppm.

3.6. Selectivity of Sensors

In the realm of CTL sensor applications, selectivity stands as a critical performance metric, particularly when detecting organic compounds, requiring a targeted molecular response [44]. This study assessed the $NiCo_2O_4$/MIL-Ti_{125} CTL sensor's selectivity in the presence of butanone, acetone, cyclohexane, n-hexane, isovaleraldehyde, formaldehyde, isovaleric alcohol, isobutanol, ethanol, methanol, n-propanol, and isopropanol, under conditions of 182 °C, 156.16 ppm and a carrier gas flow rate of 350 mL/min. Figure 12 illustrates that the sensor's response was limited to acetone, n-hexane, isovaleraldehyde, ethanol and isopropanol, exhibiting no response towards the remaining six compounds. The sensor's response to isopropanol and isovaleraldehyde was notably low, and while the signal for acetone and n-hexane was marginally higher, it did not exceed 3.33% of methanol's response intensity. These findings highlight the excellent selectivity of the $NiCo_2O_4$/MIL-Ti_{125} CTL sensor for methanol. However, there are potential interfering factors such as structural isomers (including positional isomers, functional group isomers) or stereoisomers of the target compounds [45]. For this reason, the sensing materials can be further functionalised by introducing binding sites or functional groups that interact specifically with the methanol molecule [46], in combination with the use of sensor arrays with complementary selectivity for different VOCs to achieve more accurate detection [47].

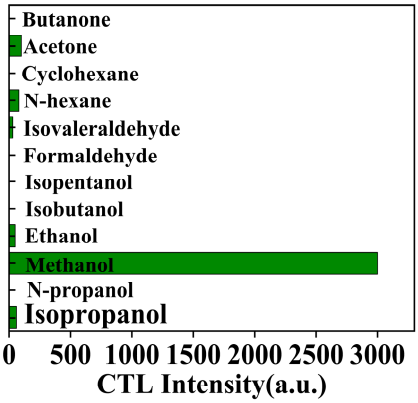
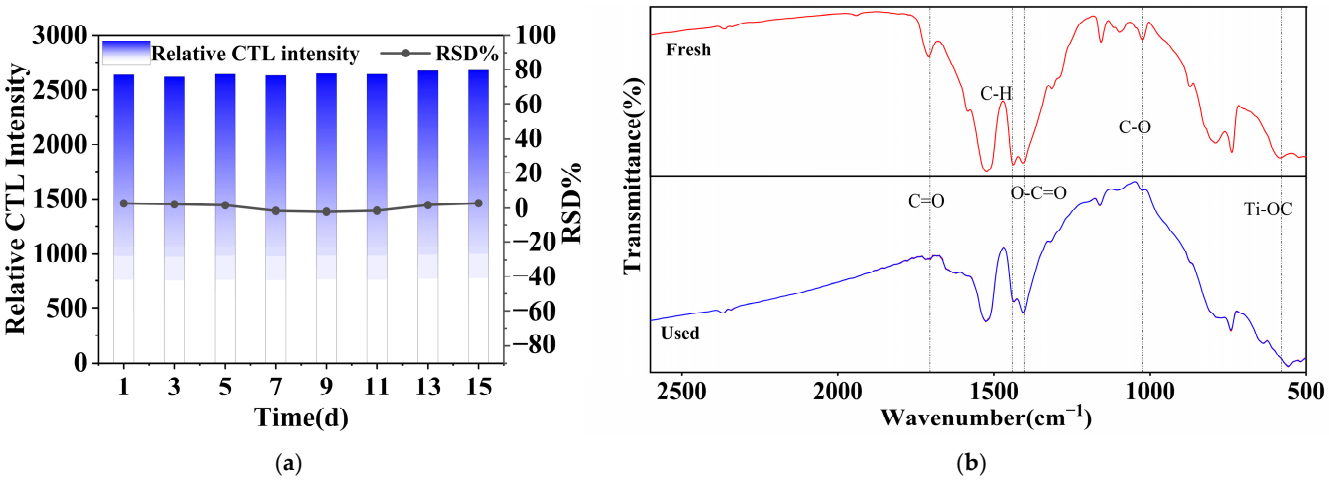


Figure 12. CTL response of the sensor to different organics (Working condition: concentration, 156.16 ppm; flow rate, 350 mL/min; temperature, 182 °C).

3.7. Stability of $NiCo_2O_4$/MIL-Ti_{125} Sensing Material for Methanol

Assessing the stability of a sensor is crucial for evaluating its performance, particularly in practical applications necessitating sustained functionality over prolonged durations [48]. In this study, experiments were performed over a two-week duration under optimal conditions, with the sensor functioning normally daily and its CTL signal strength evaluated every two days. Figure 13 displays the analytical outcomes of eight data sets selected at random over this period. The findings attesting the sensor's reproducibility, indicating minimal variability in the sensor signal strength across the eight measurements conducted

over 15 days. When compared to prior test data, the error curve for these assessments shows negligible oscillations, with a relative standard deviation (RSD) of 4.95%, which is below the 5% threshold. After the test experiment, the $NiCo_2O_4$/MIL-Ti_{125} material was also analysed by Fourier infrared analysis before and after the reaction (Figure 13b), and the results showed that although the intensity of the peaks was weakened, the peak positions were not shifted. This demonstrates that CTL sensors have the stability and durability to meet the standards of sensor applications.



(**a**) (**b**)

Figure 13. (**a**) Signal intensity and error curves for eight measurements of methanol over a two-week period; (**b**) Fourier infrared analysis of $NiCo_2O_4$/MIL-Ti_{125} material before and after reaction (Working condition: concentration, 156.16 ppm; flow rate, 350 mL/min; temperature, 215 °C).

3.8. Possible Mechanism

The XPS was utilized to characterize and analyze the elemental composition, oxidation states, and content changes of the $NiCo_2O_4$/MIL-Ti_{125} composite material before and after the CTL reaction, with the aims to investigate the impact of elemental valence state changes on the CTL process and to elucidate the underlying reaction mechanisms [49]. The XPS survey spectrum (Figure 14a) indicates that the binding energy positions of the elements remained constant before and after the reaction; however, there were shifts in peak intensities, suggesting changes in elemental content, which can be attributed to the catalytically active species. The XPS spectrum of the C 1s region depicted in Figure 14b spans the typical binding energy range of 280 to 296 eV [50]. Post-catalytic luminescence reaction, the $NiCo_2O_4$/MIL-Ti_{125} composite material exhibits an increased peak area for C-C/C=C, indicating a prevalence of carbon-carbon bonding within the material prior to the reaction. Following the reaction, there is a noticeable increase in the peak areas for both C-C/C=C and C-O, concurrent with a decrease in the O-C=O peak area, suggesting that oxidation has occurred, resulting in a reduction of carbonyl structures and the formation of additional carbon-oxygen single bonds.

In the Co 2p spectrum (Figure 15a), the characteristic peaks at 783.4 eV and 797.5 eV correspond to the Co^{2+} 2p3/2 and Co^{2+} 2p1/2 orbitals, respectively, while the peaks at 780.2 eV and 796.3 eV are associated with the Co^{3+} 2p3/2 and Co^{3+} 2p1/2 orbitals [51]. The fitting results indicate a relatively larger peak area for Co^{3+} prior to the reaction, signifying a higher proportion of Co^{3+} within the material. Post-reaction, the Co^{3+} peak area increases, and the Co^{2+} peak area diminishes, which may imply a shift in the chemical state at the material's surface or within its structure, potentially due to oxidation processes. Satellite peaks (Sat) are present in both states, with variations in their peak areas, correlating with changes in the oxidation state of cobalt.

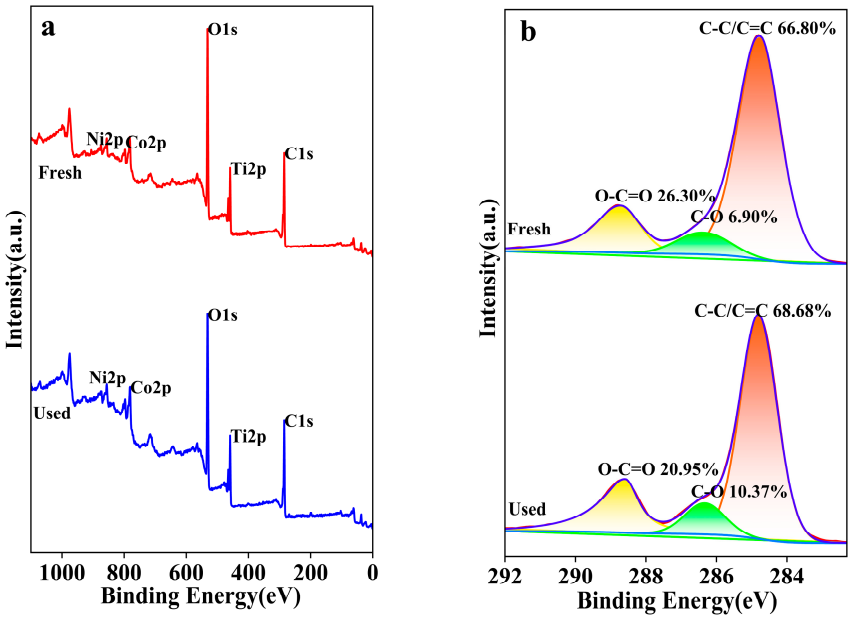


Figure 14. (**a**) $NiCo_2O_4$/MIL-Ti_{125} XPS full spectra (**b**) C1s XPS spectra.

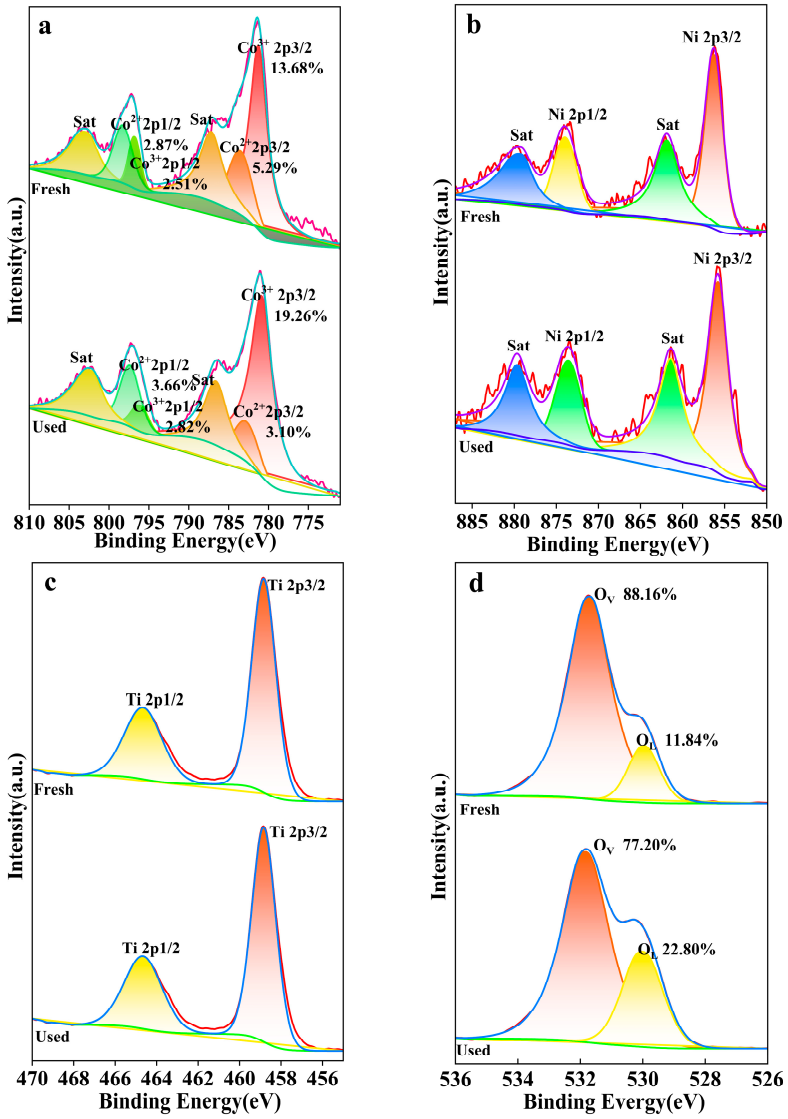


Figure 15. XPS spectra of (**a**) Co 2p, (**b**) Ni 2p, (**c**) Ti 2p and (**d**) O 1s.

The Ni 2p spectrum (Figure 15b) features peaks at 856 eV and 874.6 eV, corresponding to the Ni 2p3/2 and Ni 2p1/2 orbitals, respectively [52]. The fitting results reveal a higher initial intensity for the Ni 2p3/2 peak, suggesting a higher oxidation state of nickel within the material. Post-reaction, an increase in the Ni 2p1/2 peak intensity implies a chemical transformation at the material's surface or within its structure, potentially due to oxidation or other chemical reactions.

In the Ti 2p spectrum (Figure 15c), peaks at 459 eV and 464.6 eV correspond to the Ti 2p3/2 and Ti 2p1/2 orbitals, with a more intense peak at 458.74 eV than at 460 eV [53]. The fitting results indicate a higher initial intensity for the Ti 2p3/2 peak, suggesting a higher oxidation state of titanium in the material. An increase in the Ti 2p1/2 peak intensity post-reaction may be associated with changes in the material's chemical stability, reactivity, or surface properties during its application.

The O 1s spectrum (Figure 15d) exhibits peaks at 529.91 eV and 531.85 eV, corresponding to lattice oxygen (O_L) and oxygen vacancies (O_V) [54], respectively. The fitting results reveal a larger peak area for O_V prior to the reaction, indicating a higher quantity of oxygen vacancies within the material. Post-reaction, the O_V peak area decreases, and the O_L peak area increases, indicates that the material has reacted with oxygen to form more lattice oxygen structures. Owing to the abundance of oxygen vacancies in the $NiCo_2O_4$/MIL-Ti_{125} material, which is conducive to enhancing the CTL sensing performance.

In the CTL reaction, reductive substances such as methanol undergo oxidation reactions on the catalyst surface with oxygen, producing excited-state intermediates. These intermediates release photons as they return to their ground state, resulting in luminescence [55]. Based on sample characterization analysis and sensitivity test results, this study proposes the possible mechanism of the methanol CTL sensor as follows:

Heterojunctions can achieve spatial separation of electrons and holes on different semiconductor materials, offering strong spectral response, high charge separation efficiency, strong redox capacity, and high stability, which suggests broad application prospects in the field of CTL [56]. The heterojunction within the $NiCo_2O_4$/MIL-Ti_{125} composite partially inhibits the recombination of electrons and holes, thereby promoting the generation of electron-hole pairs and enhancing the charge carrier conversion efficiency.

The presence of oxygen vacancies is crucial for the oxygen adsorption capacity of sensing materials, increasing the types and amounts of oxygen adsorbed on the material surface, thereby promoting the conversion efficiency of CTL reactions [57]. The composite materials $NiCo_2O_4$ and MIL-Ti_{125} contain a high content of cations, and to maintain electrical neutrality, more oxygen vacancies are produced on the material surface. These oxygen vacancies help increase the adsorption of oxygen, which is then converted into different oxygen species (O^{2-}, O^-, O_2^-), among which O^- as adsorbed oxygen is an important participant in the reaction between the catalyst and oxygen, and its content determines the intensity of the reaction. Given that the analyte concentration can be varied widely, while O^- needs to be increased through oxygen vacancies [58], oxygen vacancies play an important role in improving the performance of CTL sensors.

When the $NiCo_2O_4$/MIL-Ti_{125} composite material sensing element is exposed to the air in the reaction chamber, oxygen molecules adsorb on the composite material surface to form adsorbed O_2 (ads) (Equation (2)), then O_2 gains electrons from the conduction band of the $NiCo_2O_4$/MIL-Ti_{125} composite material to become adsorbed O_2^- (Equation (3)) and adsorbed O^- (Equation (4)). When methanol is injected into the reaction chamber, the initial reactions are intensified. After the $NiCo_2O_4$/MIL-Ti_{125} composite material comes into contact with methanol molecules, the chemically adsorbed oxygen O^- on the material surface reacts with methanol molecules to produce CO_2 and H_2O (Equation (5)) [59]. The reaction-generated CO_2 is an excited-state intermediate carbon dioxide (CO_2*), and the

excited-state CO_2* molecules then return to the ground state and emit faint light, which is ultimately converted into a signal received by the sensor (Equation (6)). The overall reaction process for methanol (as shown in Figure 16) can be summarized as follows:

$$O_2\ (gas) \rightarrow O_2\ (ads) \quad (2)$$

$$O_2\ (ads) + e^- \rightarrow O_2^-(ads) \quad (3)$$

$$O_2^-\ (ads) + e^- \rightarrow 2O^-(ads) \quad (4)$$

$$CH_3CHO + 5O^- \rightarrow 2CO_2 + 2H_2O + 5e^- \quad (5)$$

$$CO_2^* \rightarrow CO_2 + h\nu \quad (6)$$

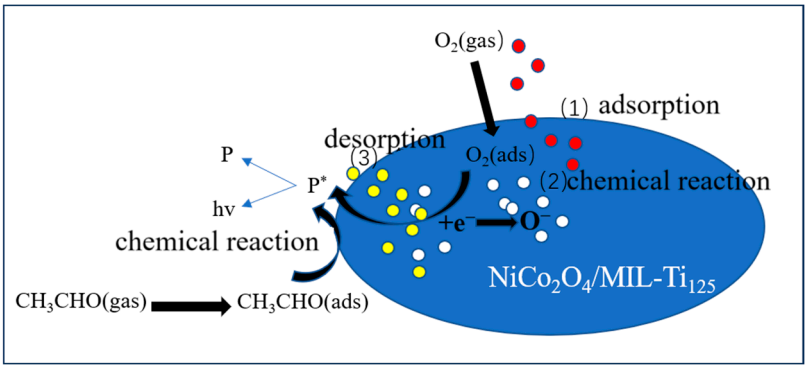


Figure 16. Schematic diagram of the three stages of the CTL response (P is an intermediate product in the reaction, and * represents the excited state of the substance.).

4. Conclusions

Within the scope of this study, a novel $NiCo_2O_4$/MIL-Ti_{125} composite material was successfully synthesized through the employment of both hydrothermal and water bath methodologies. Subsequent to its synthesis, an exhaustive examination of the material's catalytic properties was conducted, which has yielded significant insights. SEM images have revealed the presence of heterostructures around the composite material. EDS mapping has confirmed the uniform distribution of titanium (Ti), cobalt (Co), and nickel (Ni) across the material. XRD patterns have been found to align with standard references, indicating a high degree of purity in the composite. Furthermore, BET analysis has shown that the composite material possesses larger pore sizes compared to the individual $NiCo_2O_4$, which is advantageous for increased surface area and catalytic activity. The $NiCo_2O_4$/MIL-Ti_{125} composite has demonstrated exceptional performance as a low-temperature CTL sensor for methanol. The heterostructures within the material have not only improved the adsorption and reaction efficiency of methanol but also reduced the operational temperature of the sensor. Under optimized conditions, with a flow rate of 350 mL/min and a temperature of 215 °C, the CTL signal strength has been shown to be directly proportional to methanol concentrations ranging from 1 to 156.16 ppm, as described by the equation $Y = 10.388X - 4.473$ with a high correlation coefficient ($R^2 = 0.982$), and the detection limit has been determined to be as low as 0.431 ppm. The selectivity and stability of the sensor were examined, with the selectivity study demonstrating that the sensor exhibits high selectivity towards methanol, indicating its suitability for methanol detection. The relative standard deviation (RSD) of 4.95%, as determined through continuous monitoring in the stability experiment, which is an important benchmark for sensor reliability. The good CTL response of the $NiCo_2O_4$/MIL-Ti_{125} composite to methanol demonstrates its feasibility as a high-sensitivity

CTL sensing material, and our findings also provide some experimental evidence for its engineering transformation into portable methanol detection devices.

Author Contributions: Conceptualization, H.W. and B.S.; methodology, M.C., G.S. and B.S.; software, Z.S., M.C., G.S. and B.S.; validation, H.W. and B.S.; formal analysis, Z.S., M.C. and G.S.; investigation, Z.S., M.C. and G.S.; resources, H.W. and B.S.; data curation, H.W. and B.S.; writing—original draft preparation, Z.S., M.C. and B.S.; writing—review and editing, H.W., G.S. and B.S.; visualization, H.W. and B.S.; supervision, H.W. and B.S.; project administration, H.W. and B.S.; funding acquisition, H.W. and B.S.; All authors have read and agreed to the published version of the manuscript.

Funding: The authors are especially grateful to the Health Research Project of Anhui Province (AHWJ2023A20070), the Open Project Program of Anhui Institute of Urban-Rural Green Development and Urban Renewal (2304001), the Open Project Program of Anhui Institute of Strategic Study on Carbon Dioxide Emissions Peak and Carbon Neutrality in Urban-Rural Development (STY-2024-06) and the Scientific Research Start-up Foundation for Introduction of Talent, Anhui Jianzhu University (2016QD113).

Institutional Review Board Statement: Not applicable.

Informed Consent Statement: Not applicable.

Data Availability Statement: Data are contained within the article.

Conflicts of Interest: The authors declare no conflicts of interest.

References

1. Nazir, M.A.; Naseer, M.; Ullah, S.; Ahmad, K.; Ismail, M.A.; Iqbal, R.; Najam, T.; Rosaiah, P.; Raza, M.A.; Shah, S.S.A. Designing MOF-COF hybrid materials for energy, biomedical and environment applications. *Inorg. Chem. Commun.* **2024**, *170*, 113262. [CrossRef]
2. Dhiman, J.S.; Gupta, K.; Sharma, P.K. Impact of temperature-dependent viscosity on linear and weakly nonlinear stability of double-diffusive convection in viscoelastic fluid. *Chin. J. Phys.* **2024**, *92*, 1061–1077. [CrossRef]
3. Li, Q.S.; Khosravi, A.; Farsaei, A.; Sun, L. Thermodynamics, economic and carbon emission analysis of power-to-methanol process through alkaline electrolysis and monoethanolamine (MEA) carbon capture. *Chem. Eng. Sci.* **2024**, *293*, 120029. [CrossRef]
4. Arslan, M.M.; Zeren, C.; Aydin, Z.; Akcan, R.; Dokuyucu, R.; Keten, A.; Cekin, N. Analysis of methanol and its derivatives in illegally produced alcoholic beverages. *J. Forensic Leg. Med.* **2015**, *33*, 56–60. [CrossRef]
5. Ding, Y.; Zhang, L.Y.; Zhai, Y.J.; Pan, L.; Zhao, J. Provisioning optimization of construction resources: A human-centric multi-objective computational intelligence fusion approach with AI evaluation techniques. *Hum-Cent. Comput. Info.* **2024**, *14*, 63. [CrossRef]
6. Sadeghi, M.; Fakhar, M.; Hoseininejad, S.M.; Zakariaei, Z.; Sadeghi, A. The clinico-epidemiological, diagnostic and therapeutic aspects of methanol poisoning: A five-year retrospective study, northern Iran. *Drug Alcohol Depen.* **2023**, *253*, 111024. [CrossRef] [PubMed]
7. Wang, T.; Wang, B.; Huang, L.; Li, W.; Lu, Q.; Wu, H.; Liang, X.; Liu, T.; Liu, F.; Liu, F.; et al. Highly selective mixed potential methanol gas sensor based on a $Ce_{0.8}Gd_{0.2}O_{1.95}$ Solid Electrolyte and Au Sensing Electrode. *ACS Sens.* **2022**, *7*, 972–984. [CrossRef] [PubMed]
8. Magalhaes, R.; Paiva, N.; Ferra, J.M.; Magalhaes, F.D.; Martins, J.M.; Carvalho, L.H. Prediction of formaldehyde and residual methanol concentration in formalin using near infrared spectroscopy. *J. Near Infrared. Spec.* **2022**, *30*, 160–168. [CrossRef]
9. Gurkok, S. A novel carotenoid from LipT27: Production, extraction, partial characterization, biological activities and use in textile dyeing. *Arch. Microbiol.* **2022**, *204*, 296. [CrossRef]
10. Rahman, M.M.; Alam, M.M.; Asiri, A.M.; Alfaifi, S.Y.M.; Marwani, H.M. Studies of methanol electro-oxidation with ternary wet-chemically prepared ZCSO hexagonal nanodiscs with electrochemical approach. *J. Ind. Eng. Chem.* **2022**, *106*, 503–511. [CrossRef]
11. Narenderan, S.T.; Meyyanathan, S.N.; Babu, B. Review of pesticide residue analysis in fruits and vegetables. Pre-treatment, extraction and detection techniques. *Food Res. Int.* **2020**, *133*, 109141. [CrossRef] [PubMed]
12. Achir, N.; Servent, A.; Soto, M.; Dhuique-Mayer, C. Feasibility of Individual Carotenoid Quantification in Mixtures Using UV-Vis Spectrophotometry with Multivariate Curve Resolution Alternating Least Squares (MCR-ALS). *J. Spectrosc.* **2022**, *2022*, 4509523. [CrossRef]

13. Bhatta, T.; Sharma, S.; Shrestha, K.; Shin, Y.; Seonu, S.; Lee, S.; Kim, D.; Sharifuzzaman, M.; Rana, S.M.S.; Park, J.Y. Siloxene/PVDF Composite Nanofibrous Membrane for High-Performance Triboelectric Nanogenerator and Self-Powered Static and Dynamic Pressure Sensing Applications. *Adv. Funct. Mater.* **2022**, *32*, 2202145. [CrossRef]
14. Ru, J.; Zhang, R.F.; Wang, Y.X.; Ma, X.X.; Guo, Q.; Du, X.M.; Li, L.L.; Wang, Y.L. Water-stable Cd(II) metal-organic framework as multi-responsive luminescent sensor for CrO, Cr O ions and picric acid as well as its mixed matrix membranes. *J. Solid State Chem.* **2022**, *311*, 123119. [CrossRef]
15. Gao, Z.; Wang, J.X.; Muhammad, Y.; Zhang, Y.B.; Shah, S.J.; Hu, Y.; Chu, Z.; Zhao, Z.X.; Zhao, Z.X. Enhanced moisture-resistance and excellent photocatalytic performance of synchronous N/Zn-decorated MIL-125(Ti) for vaporous acetaldehyde degradation. *Chem. Eng. J.* **2020**, *388*, 124389. [CrossRef]
16. Wang, Y.Z.; Pan, Y.; Jiang, Y.; Xu, M.X.; Jiang, J.C. Wearable electrochemical gas sensor for methanol leakage detection. *Microchem. J.* **2023**, *190*, 108715. [CrossRef]
17. Ye, Q.; Dai, T.; Shen, J.; Xu, Q.; Hu, X.; Shu, Y. Incorporation of fluorescent carbon quantum dots into metal–organic frameworks with peroxidase-mimicking activity for high-performance ratiometric fluorescent biosensing. *J. Anal. Test.* **2022**, *7*, 16–24. [CrossRef]
18. Han, X.; Ai, Y.J.; Wang, L.S.; Liu, T.; Badshah, A.; Hu, X.J.; Huang, Z.T.; Mansoor, A.; Sun, W. Flexible electrochemical sensing: Compact and efficient detection of bisphenol a using copper nanoparticle decorated laser-Iinduced graphene-based electrode. *Electroanalysis* **2025**, *37*, 12025. [CrossRef]
19. Sheng, W.L.; Huang, F.W.; Lang, X.J. NH2-MIL-125(Ti)/amorphous TiO2 microspheres for enhanced visible light photocatalytic selective oxidation of amines. *Mater. Today Chem.* **2023**, *30*, 101505. [CrossRef]
20. Li, W.C.; Liu, L.Y.; Li, X.T.; Ren, H.; Zhang, L.; Parvez, M.K.; Al-Dosari, M.S.; Fan, L.M.; Liu, J.Q. A Ni(II)MOF-based hypersensitive dual-function luminescent sensor towards the 3-nitrotyrosine biomarker and 6-propyl-2-thiouracil antithyroid drug in urine. *J. Mater. Chem. B* **2024**, *12*, 11800–11809. [CrossRef] [PubMed]
21. Yang, S.X.; Xiang, X.P.; He, Z.Y.; Zhong, W.Y.; Jia, C.H.; Gong, Z.H.; Zhang, N.; Zhao, S.J.; Chen, Y. Anionic defects engineering of $NiCo_2O_4$ for 5-hydroxymethylfurfural electrooxidation. *Chem. Eng. J.* **2023**, *457*, 141344. [CrossRef]
22. Xu, Z.J.; Du, Z.Y.; Meng, Z.S.; Zhang, R.L.; Zeng, F.D.; Xu, J.; Long, B.H.; Tian, H.W. A novel template processing method for preparing spinel oxides with various morphologies to assemble high-performance supercapacitors. *J. Alloys Compd.* **2023**, *955*, 170284. [CrossRef]
23. Tian, G.; Lin, J.Y.; Zhou, Y.; Huang, Z.Y.; Wei, X.P.; Li, J.P. Development of a molecularly imprinted photochemical sensor based on Bi_2O_3/TiO_2 NTs heterojunction extended-gate field-effect transistor for the determination of trace neomycin. *Microchem. J.* **2023**, *193*, 108983. [CrossRef]
24. Liu, G.Q.; Cheng, Y.W.; Qiu, M.Q.; Li, C.C.; Bao, A.Y.; Sun, Z.T.; Yang, C.Z.; Liu, D.M. Facilitating interface charge transfer via constructing NiO/NiCo O heterostructure for oxygen evolution reaction under alkaline conditions. *J. Colloid Interface Sci.* **2023**, *643*, 214–222. [CrossRef] [PubMed]
25. Xu, M.S.; Zhu, P.F.; Cai, Q.H.; Bu, M.C.; Zhang, C.H.; Wu, H.; He, Y.Z.; Fu, M.; Li, S.Q.; Liu, X.Y. Fabrication of TiO/NH-MIL-125(Ti) MOF-driven strategy to promote efficient interfacial effects for enhancing photocatalytic NO removal activity. *Chin. Chem. Lett.* **2024**, *35*, 109524. [CrossRef]
26. Huang, F.; Humayun, M.; Li, G.; Fan, T.T.; Wang, W.L.; Cao, Y.L.; Nikiforov, A.; Wang, C.D.; Wang, J. Z-scheme Bi O Br/NH-MIL-125(Ti) heterojunctions enable exceptional visible photocatalytic degradation of organic pollutant. *Rare Metals* **2024**, *43*, 3161–3172. [CrossRef]
27. Wang, H.Y.; Shi, X.Q.; Liu, F.; Duan, T.M.; Sun, B. Non-invasive rapid detection of lung cancer biomarker toluene with a cataluminescence sensor based on the two-dimensional nanocomposite $Pt/Ti_3C_2T_x$-CNT. *Chemosensors* **2022**, *10*, 333. [CrossRef]
28. Miti, T.; Pan, H.; Wickline, S.A. New Approach in Characterize siRNA Delivery Platform for Clinical Translation. *FASEB J.* **2018**, *32*, 570.1. [CrossRef]
29. Ghani, F.; Haidry, A.A.; Raza, A.; Fatima, Q.; Weng, Y.L.; Sajjad, M.; Albaqami, M.D.; Mohammad, S. Anisotropic CO adsorption and enhanced O activation on defective TiS monolayer: A DFT study. *Mater. Today Commun.* **2024**, *40*, 109680. [CrossRef]
30. Duan, Z.H.; Li, J.; Yuan, Z.; Jiang, Y.D.; Tai, H.L. Capacitive humidity sensor based on zirconium phosphate nanoplates film with wide sensing range and high response. *Sens. Actuators B Chem.* **2023**, *394*, 134445. [CrossRef]
31. Alatawi, O.M. Recycling and breakdown photodegradation processes cost of BEN-TiQD via different photodegradation processes of brilliant green S dye and industrial effluents. *Ceram. Int.* **2024**, *50*, 53960–53969. [CrossRef]
32. Babaei, S.; Ghasemzadeh, H.; Tesson, S. Methane adsorption of nanocomposite shale in the presence of water: Insights from molecular simulations. *Chem. Eng. J.* **2023**, *475*, 146196. [CrossRef]
33. Hajji, M.; Dabbabi, S.; Ajili, M.; Jebbari, N.; Loureiro, A.G.; Kamoun, N.T. Investigations on physical properties of CuO-ZnO couple oxide sprayed thin films for environmental applications (ozone gas sensing and MB degradation). *J. Mater. Sci. Mater. Electron.* **2024**, *35*, 633. [CrossRef]

34. Subhan, M.A.; Saha, P.C.; Alam, M.M.; Asiri, A.M.; Raihan, T.; Uddin, J.; Ghaan, W.; Azad, A.K.; Al-Mamun, M.; Nakata, H.; et al. NIR red luminescent doped Ag·$(Y_{0.95}$ $Eu_{0.05})_2O_3$ nanocomposite for 3-Chlorophenol sensor probe and anti-MDR bacterial application. *J. Environ. Chem. Eng.* **2021**, *9*, 106881. [CrossRef]
35. Cao, H.R.; Mao, K.; Zhang, H.; Wu, Q.Q.; Ju, H.X.; Feng, X.B. Thermal stability and micrdose-based coupling CRISPR/Cas12a biosensor for amplification-free detection of hgcA gene in paddy soil. *Sci. Total Environ.* **2024**, *909*, 168536. [CrossRef] [PubMed]
36. Bagul, V.R.; Bhagure, G.R.; Tayde, D.T. Effect of Cobalt Doping on Gas Sensing Properties of SnO_2 Thick Films Prepared by Chemical Co-Precipitation Method. *Asian J. Chem.* **2023**, *35*, 2911–2916. [CrossRef]
37. Haiouani, K.; Hegazy, S.; Alsaeedi, H.; Bechelany, M.; Barhoum, A. Green Synthesis of Hexagonal-like ZnO Nanoparticles Modified with Phytochemicals of Clove (Syzygium aromaticum) and Extracts: Enhanced Antibacterial, Antifungal, and Antioxidant Activities. *Materials* **2024**, *17*, 4340. [CrossRef] [PubMed]
38. Mamat, M.H.; Parimon, N.; Ismail, A.S.; Banu, I.B.S.; Basha, S.S.; Vijayaraghavan, G.V.; Yaakob, M.K.; Suriani, A.B.; Ahmad, M.K.; Rusop, M. Structural, optical, and electrical evolution of sol-gel-immersion grown nickel oxide nanosheet array films on aluminium doping. *J. Mater. Sci. Mater. Electron.* **2019**, *30*, 9916–9930. [CrossRef]
39. Saravanan, P.; Gotipamul, P.P.; Damodarreddy, K.; Campos, C.H.; Selvaraj, A.; Mangalaraja, R.V.; Chidambaram, S. Synthesis of isolated ZnO nanorods on introducing g-C_3N_4 for improved photoelectrocatalytic methanol production by CO_2 reduction. *Inorg. Chem. Commun.* **2024**, *170*, 113313. [CrossRef]
40. Serrar, H.; Bouabellou, A.; Bouachiba, Y.; Taabouche, A.; Bouhank, A.; Bellal, Y.; Merabti, H. Effect of water and methanol solvents on the properties of CuO thin films deposited by spray pyrolysis. *Thin Solid Films* **2019**, *686*, 137282. [CrossRef]
41. Chen, L.; Zhang, J.; Qin, H.Y. Fabrication of three dimensional graphene/carbon nanotube/copper foam field emitter by electrophoretic deposition and its emission properties. *Chem. Phys. Lett.* **2024**, *838*, 141101. [CrossRef]
42. Wu, Y.J.; Lin, Z.C.; Chen, N.; Wang, J.X.; Zhang, R.K. Lanthanum oxycarbonate with nanosheet-like network structure for cataluminescence sensing of tetrahydrofuran. *Microchem. J.* **2022**, *181*, 107710. [CrossRef]
43. Kumar, A.; Rana, S.; Sharma, G.; Dhiman, P.; Shekh, M.I.; Stadler, F.J. Recent advances in zeolitic imidazole frameworks based photocatalysts for organic pollutant degradation and clean energy production. *J. Environ. Chem. Eng.* **2023**, *11*, 110770. [CrossRef]
44. Shi, G.L.; Hu, G.P.; Gu, L.C.; Rao, Y.; Zhang, Y.X.; Ali, F. Cataluminescence sensor based on $LaCO_3OH$ microspheres for volatile organic compounds detection and pattern recognition. *Sens. Actuators B Chem.* **2024**, *403*, 135177. [CrossRef]
45. Zhang, X.; Dai, Y.; Sun, J.; Shen, J.; Lin, M.; Xia, F. Solid-state nanopore/nanochannel sensors with enhanced selectivity through pore-in modification. *Anal. Chem.* **2024**, *96*, 2277–2285. [CrossRef] [PubMed]
46. Talukder, N.; Wang, Y.; Tong, X.; Lee, E.S. Chemical changes from N-doped graphene and metal-organic frameworks to N-G/MOF composites for improved electrocatalytic activity. *Carbon* **2025**, *232*, 119816. [CrossRef]
47. Mei, H.X.; Peng, J.Y.; Wang, T.; Zhou, T.T.; Zhao, H.R.; Zhang, T.; Yang, Z. Overcoming the limits of cross-sensitivity: Pattern recognition methods for chemiresistive gas sensor array. *Nano-Micro Lett.* **2024**, *16*, 293–349. [CrossRef]
48. Yan, Q.; Chen, S.Y.; Shi, H.F.; Wang, X.F.; Meng, S.H.; Li, J.P. Fabrication of polymer-derived SiBCN ceramic temperature sensor with excellent sensing performance. *J. Eur. Ceram. Soc.* **2023**, *43*, 7373–7380. [CrossRef]
49. Chen, H.; Wu, Y.F.; Guo, H.; Li, S.; Cheng, H.L.; Wen, C.X.; Zhao, Z.Q.; Lu, X.W. Characteristic and mechanism of efficient phosphate removal by Portland cement/slag powder/coal ash-hydrate (PC/SP/CA-H). *J. Environ. Chem. Eng.* **2024**, *12*, 112372. [CrossRef]
50. Priya, D.D.; Surendra, T.V.; Shajahan, S.; Muthuraja, S.; Roopan, S.M. Design and sustainable production of natural carbon incorporated CuO/C nanocomposite using biomass. *Biomass Convers. Biorefin.* **2023**, *14*, 25223–25237. [CrossRef]
51. Li, L.A.; Fang, S.; Chen, W.; Li, Y.Y.; Vafadar, M.F.; Wang, D.H.; Kang, Y.; Liu, X.; Luo, Y.M.; Liang, K.; et al. Facile Semiconductor p-n Homojunction Nanowires with Strategic p-Type Doping Engineering Combined with Surface Reconstruction for Biosensing Applications. *Nano-Micro Lett.* **2024**, *16*, 192. [CrossRef]
52. Huang, Z.Y.; Liao, M.; Zhang, S.F.; Wang, L.X.; Gao, M.C.; Luo, Z.Y.; Isimjan, T.T.; Wang, B.; Yang, X.L. Valence electronic engineering of superhydrophilic Dy-evoked Ni-MOF outperforming RuO_2 for highly efficient electrocatalytic oxygen evolution. *J. Energy Chem.* **2024**, *90*, 244–252. [CrossRef]
53. Li, R.Q.; Bian, Y.J.; Yang, C.M.; Guo, L.; Ma, T.X.; Wang, C.T.; Fu, F.; Wang, D.J. Electronic structure regulation and built-in electric field synergistically strengthen photocatalytic nitrogen fixation performance on Ti-BiOBr/TiO heterostructure. *Rare Metals* **2024**, *43*, 1125–1138. [CrossRef]
54. Xu, Q.; Wang, S.Y.; Xu, C.M.; Chen, X.Y.; Zeng, S.W.; Li, C.Y.; Zhou, Y.; Zhou, T.H.; Niu, Y.C. Synergistic effect of electrode defect regulation and Bi catalyst deposition on the performance of iron-chromium redox flow battery. *Chin. Chem. Lett.* **2023**, *34*, 108188. [CrossRef]
55. Hu, J.X.; Zhang, L.C.; Lv, Y. Recent advances in cataluminescence gas sensor: Materials and methodologies. *Appl. Spectrosc. Rev.* **2019**, *54*, 306–324. [CrossRef]

56. Kumar, S.; Mirzaei, A.; Kumar, A.; Lee, M.H.; Ghahremani, Z.; Kim, T.U.; Kim, J.Y.; Kwoka, M.; Kumar, M.; Kim, S.S.; et al. Nanoparticles anchored strategy to develop 2D MoS_2 and $MoSe_2$ based room temperature chemiresistive gas sensors. *Coordin. Chem. Rev.* **2024**, *503*, 215657. [CrossRef]
57. Wong, J.S.; Onizhuk, M.; Nagura, J.; Thind, A.S.; Bindra, J.K.; Wicker, C.; Grant, G.D.; Zhang, Y.X.; Niklas, J.; Poluektov, O.G.; et al. Coherent Erbium Spin Defects in Colloidal Nanocrystal Hosts. *ACS Nano* **2024**, *18*, 19110–19123. [CrossRef] [PubMed]
58. Yang, J.; Hu, J.F.; Zhang, W.H.; Han, H.W.; Chen, Y.H.; Hu, Y. The opportunities and challenges of ionic liquids in perovskite solar cells. *J. Energy Chem.* **2023**, *77*, 157–171. [CrossRef]
59. Xing, X.; Zhao, T.; Cheng, J.; Duan, X.X.; Li, W.P.; Li, G.G.; Zhang, Z.S.; Hao, Z.P. Promotional effect of Cu additive for the selective catalytic oxidation of-butylamine over CeZrO catalyst. *Chin. Chem. Lett.* **2022**, *33*, 3065–3072. [CrossRef]

Disclaimer/Publisher's Note: The statements, opinions and data contained in all publications are solely those of the individual author(s) and contributor(s) and not of MDPI and/or the editor(s). MDPI and/or the editor(s) disclaim responsibility for any injury to people or property resulting from any ideas, methods, instructions or products referred to in the content.